Sustainable Energy & Fuels

ROYAL SOCIETY OF CHEMISTRY

PAPER

View Article Online
View Journal

Cite this: DOI: 10.1039/d4se01074d

FeNi bimetallic oxides derived from MOFs as precursors promote efficient electrochemical synthesis of ammonia†

Jiuqing Xiong, Yanli Zhang, Yifan Wang, Haoyu Zhang, Shengwei Huang, Shihai Yan * and Bingping Liu*

In recent years, electrochemical nitrate reduction (NO_3^-RR) for ammonia synthesis has garnered increasing attention as a sustainable alternative to the Haber–Bosch process for ammonia production and wastewater treatment. The development of efficient electrocatalysts is crucial because the activity and selectivity for ammonia production remain relatively low. In this letter, we conducted rational design and density functional theory (DFT) calculations, and obtained a high-yield and efficient catalyst, $NiFe_2O_4$. The catalyst exhibits a yield rate of 21.45 mg h^{-1} cm^{-2} and a faradaic efficiency of 97.65%, surpassing the performance of most Fe-based and Ni-based catalysts. Experimental results demonstrate that different calcination temperatures and the introduction of varying amounts of nickel precursors significantly affect the catalyst's performance, as is further supported by DFT calculations. This study offers a promising strategy for designing high-performance NO_3^-RR catalysts for electrocatalytic NH_3 synthesis and waste water treatment.

Received 5th August 2024
Accepted 7th November 2024

DOI: 10.1039/d4se01074d

rsc.li/sustainable-energy

1. Introduction

As one of the most crucial chemical products in modern society, ammonia (NH_3) serves not only as an indispensable raw material in various industries, including agriculture, metallurgy, textiles, and pharmaceuticals, but also is considered to be a carbon-neutral energy carrier and an efficient energy storage medium due to its high energy density.[1–6] However, the predominant method for industrial ammonia synthesis at present is still the Haber–Bosch process, which operates at high temperatures ranging from 400 to 600 degrees Celsius and under high pressures of 200 to 350 atmospheres. This process consumes a substantial amount of energy and releases significant quantities of greenhouse gases. Therefore, there is an urgent need to explore green and sustainable alternatives for ammonia synthesis.[7–11] The emerging electrocatalytic reduct2ion of nitrogen (N_2) to produce NH_3 (NRR) has appropriately reduced energy consumption and carbon emission.[12,13] However, due to the strongly competitive hydrogen evolution reaction (HER), very low solubility of N_2, and the intense N≡N bond (945 kJ mol^{-1}), the NH_3 yield and faradaic efficiency (FE) are significantly lower, even at high current densities, compared to the yields achieved by the Haber–Bosch process.[14–17] In recent times, there has been a growing interest in the electrocatalytic reduction of nitrate to ammonia due to its higher efficiency, with lower energy consumption (204 kJ mol^{-1} for N═O bond cleavage), and the unlimited solubility of nitrate ions (NO_3^-).[18–23] Furthermore, NO_3^- is a common environmental pollutant, abundant in industrial and sanitary wastewater. With the rapid development of industrial production, agricultural activities, and the increasing human population, nitrate pollution in water bodies has become increasingly severe. This leads to water eutrophication, causing damage to ecosystems and posing threats to human health. Therefore, the conversion of discarded NO_3^- into value-added ammonia is evidently a strategy of "turning waste into treasure".[24–28]

However, the reduction of nitrate to produce ammonia is a complex process involving the transfer of 9 protons and 8 electrons, which leads to the formation of by-products, including NO_2^-, NO, N_2, and N_2O.[29–31] Moreover, this process competes with the two-electron HER, ultimately resulting in diminished NH_3 yields and FE.[16,29,32] The critical factor in the electrochemical reduction of nitrate is the design of the catalyst. Therefore, seeking innovative catalyst materials that can overcome these challenges is crucial for practical applications. Consequently, there has been extensive exploration of diverse catalyst materials, including metals, alloys, metal oxides, metal sulfides, and non-metals.[1,7,21,26,30] Among metal materials, iron (Fe) has exhibited high activity and selectivity in the reduction of NO_3^- to NH_3. Fe is the most widely distributed transition metal element in the natural world, and possesses unique advantages (inexpensive and readily available, low cost, non-toxic, and harmless). In addition, Fe is a fundamental

---

College of Chemistry and Pharmaceutical Sciences, Qingdao Agricultural University, Qingdao, 266109, China. E-mail: shyan@qau.edu.cn; bpliu@qau.edu.cn

† Electronic supplementary information (ESI) available. See DOI: https://doi.org/10.1039/d4se01074d

component present in virtually all nitrogenases, playing a pivotal role as an active center during electron transfer processes.[33–35] Nickel (Ni) possesses significant O–H activation capability and strong adsorption ability for hydrogen (H*). In the process of nitrate reduction, it promotes the depletion of H*, favoring H* consumption over excessive HER, thereby providing sufficient active hydrogen and significantly inhibiting HER.[36–39]

Metal–organic frameworks (MOFs) have attracted extensive attention as a burgeoning class of electrocatalytic materials, owing to their abundance of unsaturated metal sites, exceptionally high surface area, and versatile open and tunable porous structures.[40–45] However, pure MOFs face challenges such as insufficient conductivity.[46] In comparison to pure MOFs as electrocatalysts, structures derived from MOFs precursors can exhibit excellent electrocatalytic performance.[46,47] By forming hollow nanocage structures, the number of active sites can be significantly increased, and mass transfer is also enhanced. This is typically achieved through processes such as etching treatment, thermal treatment, and secondary growth treatment to create hollow structures.[47–51] Therefore, we explore the enhancement of Fe-based MOFs in the NO_3^- reduction to NH_3 process by introducing a Ni source. Through the oil bath method, a Ni source is introduced to etch pure MOFs. This results in the formation of hollow nano-cage Fe–Ni layered double hydroxide (Fe–Ni-LDH) structures. As compared with that (yield: 11.05 mg h^{-1} cm^{-2}, FE: 92.54%) of pure Fe MOFs, the NH_3 yield and FE (yield: 15.67 mg h^{-1} cm^{-2}, FE: 93.00%) of Fe–Ni-LDH are enhanced.

Transition metal oxides with spinel-type bimetallic structures have attracted significant interest due to their unique crystal structure, multifunctional ion arrangement, multivalent composition, and high conductivity.[52,53] Spinel-type bimetallic oxides, such as $FeCo_2O_4$, $MnCo_2O_4$, and $NiFe_2O_4$, have been extensively employed in the realm of electrocatalysis.[54,55] Particularly, Zhang *et al.* synthesized $NiFe_2O_4$, which exhibited excellent yields in the electrocatalytic NO_3^- reduction.[56] Therefore, we further annealed the synthesized Fe–Ni-LDH in the nitrogen atmosphere, resulting in the formation of a spinel-type $NiFe_2O_4$ nanocage. This leads to a notable enhancement of both NH_3 yield and FE (yield: 21.45 mg h^{-1} cm^{-2}, FE: 97.63%). In this study, we experimentally investigated the impact of varying nickel ratios and different calcination temperatures on the catalytic performance. Additionally, we delved deeper into the mechanistic understanding of different nickel ratios through theoretical calculations using the VASP simulation package.[57]

2. Method and experimental

2.1. Materials

Ferric chloride hexahydrate ($FeCl_3 \cdot 6H_2O$, ≥99%), potassium nitrate (KNO_3, ≥99%), sodium nitroferricyanide ($C_5FeN_6Na_2O \cdot 2H_2O$, ≥98%), sulfonamide ($C_6H_8N_2O_2S$, ≥99.8%) were all procured from China National Pharmaceutical Group Corporation. Sodium hydroxide (NaOH, ≥96%), salicylic acid ($C_7H_6O_3$, ≥99.5%), and ethanol were obtained from Laiyang Kangde Chemical Co., Ltd (China). Nickel chloride hexahydrate ($NiCl_2 \cdot 6H_2O$, ≥98%) was purchased from Laiyang Economic and Technological Development Zone Fine Chemical Factory (China). Sodium citrate ($C_6H_5Na_3O_7$, ≥99%), sodium hypochlorite (NaClO, ≥10%), *N*,*N*-dimethylformamide (C_3H_4NO, ≥99.5%) were acquired from Tianjin Bodi Chemical Co., Ltd, Tianjin Yongda Chemical Reagent Co., Ltd, and Tianjin Fuyu Fine Chemical Co., Ltd, respectively. *N*-(1-naphthyl) ethylenediamine dihydrochloride (≥99.8%) was procured from Tianjin Aopson Chemical Co., Ltd. Phosphoric acid (H_3PO_4, ≥99%) was obtained from Beijing Chemical Industry Co., Ltd. Phthalic acid ($C_8H_6O_4$, ≥99%) was purchased from Shanghai Maclin Biochemical Technology Co., Ltd.

2.2. Catalyst synthesis

2.2.1. Synthesis of Fe MOFs. $FeCl_3 \cdot 6H_2O$ and phthalic acid were dissolved in 40 mL of *N*,*N*-dimethylformamide, and the mixture was vigorously stirred magnetically for 1 hour. The resulting solution was moved into a stainless-steel autoclave equipped with a polytetrafluoroethylene coating and heated at 120 °C for 15 hours. After cooling to room temperature, the product was collected by centrifugation and washed multiple times with ultrapure water and anhydrous ethanol. Finally, Fe MOFs were obtained by drying overnight in oven at 60 °C.

2.2.2. Synthesis of Fe–Ni LDH. 0.36 mmol Fe MOFs and 0.86 mmol $NiCl_2 \cdot 6H_2O$ were separately dissolved in 25 mL of anhydrous ethanol and stirred until well-mixed. After achieving uniform mixing, the two solutions were combined in a round-bottom flask and heated in a 30 °C oil bath for 3 hours. After cooling to room temperature, the resulting mixture was washed several times with ultrapure water and anhydrous ethanol. Finally, the Fe–Ni LDH was obtained by drying overnight in an oven at 60 °C. By adjusting the nickel ratio, Fe–Ni LDH with different proportions was obtained.

2.2.3. Synthesis of $NiFe_2O_4$. The Fe–Ni LDH was calcined in a tube furnace under a nitrogen atmosphere for 2 hours. The tube furnace was heated at a rate of 1° per minute. By adjusting different calcination temperatures, $NiFe_2O_4$ samples were obtained at temperatures of 300 °C, 350 °C, and 400 °C, respectively.

2.3. Characterization of samples

The morphology and microstructure of the catalyst were analyzed using scanning electron microscopy (SEM, ZEISS Gemini SEM 300). The catalyst element analysis was conducted using energy-dispersive X-ray spectroscopy (ZEISS Gemini SEM 300). The crystal structure of the catalyst was characterized by X-ray diffraction (XRD, Rigaku Smart Lab SE). Additionally, the chemical composition and state of the catalyst surface were determined by X-ray photoelectron spectroscopy (XPS, Thermo Scientific K-Alpha). The concentration of NH_3 was measured with a UV-3900 spectrophotometer.

2.4. Preparation of the working electrode

Three milligrams of the catalyst were weighted and placed into a centrifuge tube. Forty microliters of Nafion solution and 500 microliters of isopropanol were added. Ultrasonication was applied for 1 hour to ensure thorough mixing. One hundred microliters of the catalyst after ultrasonication were taken, and it was deposited onto a carbon cloth (0.5 cm × 1 cm), ensuring that the catalyst loading area on the carbon cloth was 0.2 cm^2. After drying, it was secured onto an electrode clamp to create the working electrode.

2.5. Electrochemical measurements

Electrochemical tests were conducted in an H-type electrolytic cell. The cell was separated by a Nafion-117 membrane. Prior to the tests, electrolyte solutions of 30 mL 0.1 M NaOH and 0.1 M KNO_3 were added to the respective sides of the electrolytic cell. Argon gas was then introduced into the cathodic electrolytic cell for 15 minutes before testing to remove residual air from the system. Argon gas flow was maintained throughout the testing period. In this three-electrode system, the electrode supporting the catalyst served as the working electrode, while saturated Ag/AgCl and a platinum sheet functioned as the counter and reference electrodes, respectively. All potentials were converted to the reversible hydrogen electrode potential using the reference scalar: E (*vs.* RHE) = E (*vs.* Ag/AgCl) + 0.059 pH + 0.197 V.

2.6. Determination of NH_3, NO_2^- and N_2H_4

The concentration of NH_3 was determined using the indophenol blue spectrophotometric method. Two milliliters of the catholyte, diluted tenfold, were mixed successively with 2 mL of a 1 M NaOH solution containing 5 wt% salicylic acid and 5 wt% sodium citrate, 1 mL of 0.05 M NaClO solution, and 0.2 mL of a 1 wt% $C_5FeN_6Na_2O$ solution. After a 2 hours incubation at room temperature, the absorbance was measured at a wavelength of 655 nm using a UV-vis spectrophotometer. The obtained absorbance value was then used to determine the NH_3 concentration in the electrolyte through a concentration-absorbance standard curve.

Initially, 2.94 mL of H_3PO_4 was added to 50 mL of H_2O. Subsequently, 0.1 g of *N*-(1-naphthyl) ethylenediamine dihydrochloride and 1 g of sulfonamide were weighed and introduced into the mixture of H_3PO_4 and H_2O. The resulting color reagent was thoroughly mixed. Next, 1 mL of the diluted electrolyte was taken, and 4 mL of ultrapure water along with 0.1 mL of the color reagent were added. Lastly, the mixed solution was allowed to stand for 20 minutes, and the absorbance at a wavelength of 540 nm was measured using a UV-vis absorption spectrophotometer. The NO_2^- concentration was determined through analysis utilizing a standard curve.

First, the color reagent was prepared by combining *p*-$C_9H_{11}NO$ (2.99 g), HCl (15 mL), and C_2H_5OH (150 mL). Next, 1 mL of catholyte and 1 mL of the color reagent were added to a centrifuge tube. The mixture was then left to stand for 20 minutes before being analyzed using a UV-vis spectrophotometer. Finally, the concentration was determined by comparing it to the N_2H_4 standard curve.

2.7. Computational details

In this research, density functional theory (DFT) calculations were performed on $NiFe_2O_4$ using the first-principles computational simulation package (VASP 5.4.4).[57] This software was developed by the Hafner group. The structural optimization and electronic energy calculations for $NiFe_2O_4$ utilized the generalized gradient approximation of the Perdew–Burke–Enzzerhof (GGA-PBE) exchange–correlation functional, incorporating the projector augmented wave (PAW) method for pseudopotential determination. Brillouin zone gamma points were sampled through a (3 × 3 × 1) Monkhorst–Pack *k*-point grid. Simultaneously, a cutoff energy of 500 electron volts was applied, maintaining self-consistent calculations with a total energy convergence criterion of 10^{-5} eV electron volts and a force convergence criterion of -0.05 eV $Å^{-1}$ per atom. To consider van der Waals interactions and adsorption energy of each intermediate on the catalyst, the DFT-D2 method was applied for $NiFe_2O_4$. The formula for calculating the Gibbs free energy (ΔG): $\Delta G = \Delta E + \Delta ZPE - T\Delta S$, where ΔE represents electronic energy, ΔZPE denotes zero-point correction energy, T is the reaction temperature, and ΔS signifies the entropy change.

3. Results and discussion

3.1. Synthesis and characterizations of catalysts

$NiFe_2O_4$ was primarily synthesized *via* a three-step method, as depicted in Fig. S1.† Initially, Fe MOFs were synthesized following previously reported methods.[58] Subsequently, 0.36 mmol of Fe MOFs was mixed with 0.86 mmol of $NiCl_2 \cdot 6H_2O$ in ethanol and heated in an oil bath at 30 °C for 3 hours, yielding Fe–Ni LDH, which was calcined in a tube furnace under N_2 atmosphere for 2 hours, with the temperature ramped up at a rate of 1 °C per minute. By varying the calcination temperature, $NiFe_2O_4$ was obtained at temperatures of 300 °C, 350 °C, and 400 °C, respectively.

The scanning electron microscopy (SEM) images show that the synthesized Fe MOFs exhibit a tetrahedral morphology (Fig. 1a), consistent with the previously reported morphology, confirming successful synthesis of Fe MOFs. In Fig. 1b and c, it is evident that the subsequent formation of Fe–Ni LDH upon modification of Fe MOFs. $NiFe_2O_4$ retains the essential morphology and framework of the original MOFs, thus preserving the advantages of the MOFs material while obtaining additional active sites, which corresponds to the superior catalytic performance of $NiFe_2O_4$ reported later as compared to Fe MOFs and Fe–Ni LDH in NO_3^-RR.

By adjusting the proportion of nickel added, Fe–Ni LDH with different ratios were obtained. In Fig. S2,† $NiFe_2O_4$ obtained through calcination at 350 °C after etching with 0.43 mmol, 0.86 mmol, and 1.29 mmol Ni, respectively, exhibits varying morphologies. When 1.29 mmol Ni is used, the etching of Fe MOFs is particularly severe, causing significant framework collapse. For both 0.43 mmol and 0.86 mmol Ni, the etching degree is relatively weak, preserving the original MOF structure. With 0.86 mmol Ni, the etching of Fe MOFs is more pronounced as compared to that of 0.43 mmol, resulting in higher exposure of active sites. This is consistent with the experimental results that, compared with the samples containing 0.43 mmol and 1.29 mmol Ni, the sample containing 0.86 mmol Ni exhibits

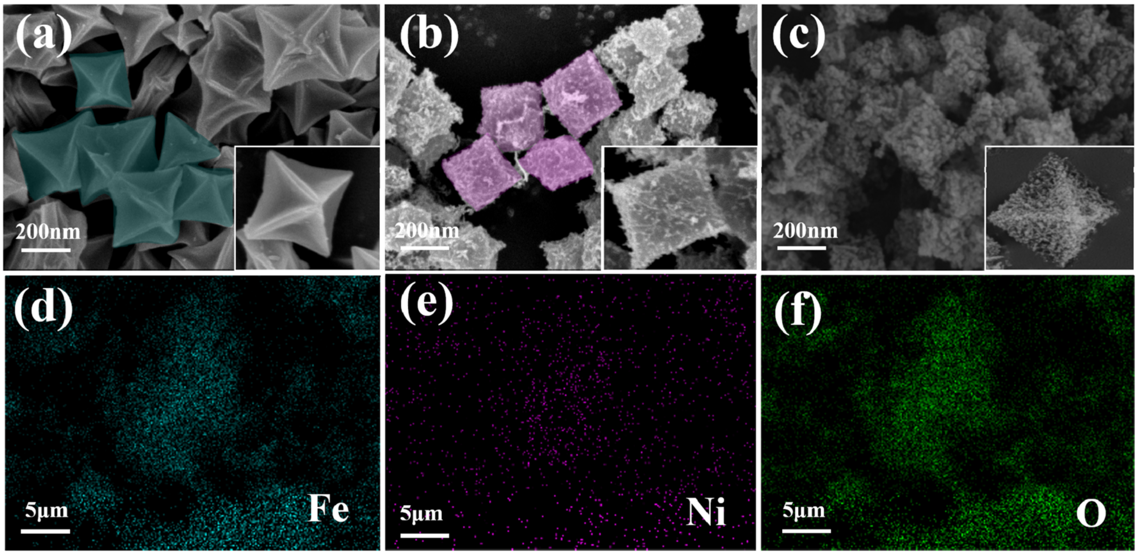

Fig. 1 SEM of (a) Fe MOFs, (b) Fe–Ni LDH nanoparticles, (c) $NiFe_2O_4$ nanoparticles, (d–f) EDS mapping images of $NiFe_2O_4$.

better catalytic performance in NO_3^-RR. Fig. S3† shows the morphologies of Fe MOFs etched with 0.86 mmol Ni and subsequently calcined at 300 °C, 350 °C, and 400 °C, respectively. At 400 °C, the framework of Fe MOFs collapses severely, losing the original function of the MOFs framework. At 350 °C, compared to 300 °C, MOFs exhibit more severe decomposition while maintaining the original morphology and exposing more active sites. This corresponds to the subsequent results regarding the optimal catalytic performance at 350 °C.

To clarify the crystal structure of $NiFe_2O_4$, the X-ray diffraction (XRD) spectra are obtained (Fig. 2a). The analysis reveals that the synthesized $NiFe_2O_4$ aligns well with the spinel phase arrangement (JCPDS no. 10-0325). The diffraction peaks observed at 18.4°, 30.3°, 35.7°, 37.3°, 43.4°, 53.8°, 57.4°, 62.9°, and 74.6°

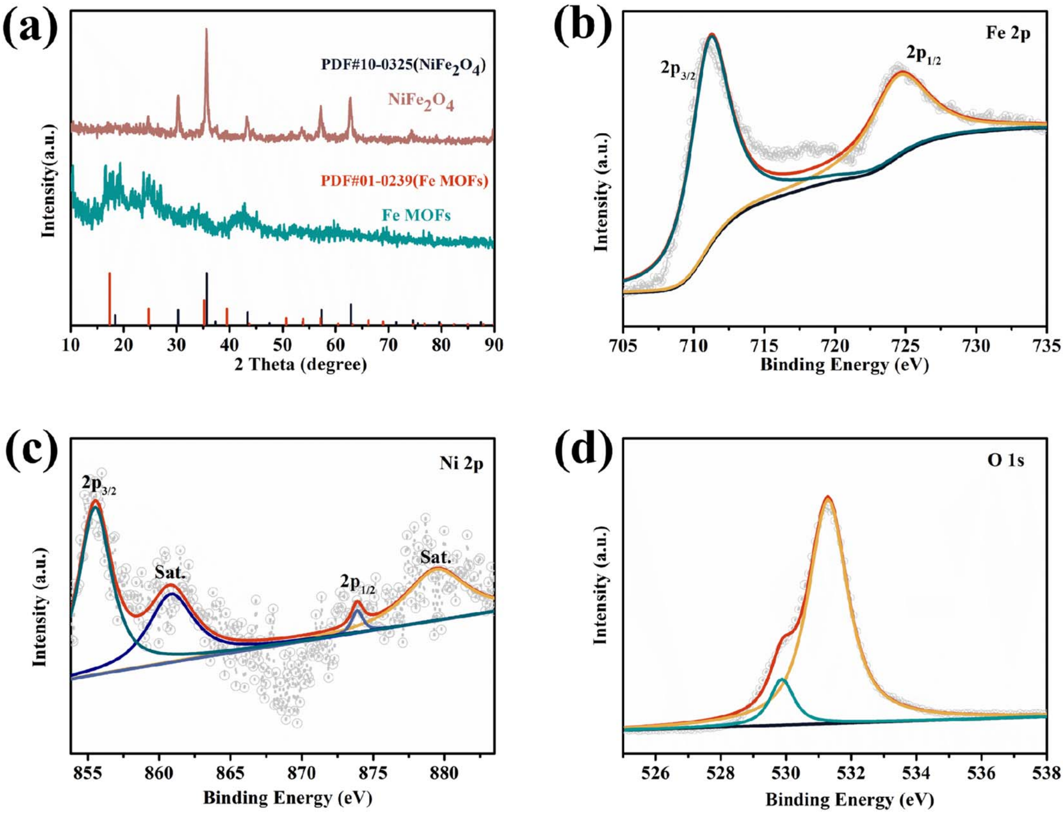

Fig. 2 (a) XRD patterns of $NiFe_2O_4$, (b–d) The XPS of $NiFe_2O_4$ measured spectra are Fe 2p, Ni 2p and O 1s.

correspond to the (111), (220), (311), (222), (400), (422), (511), (440), and (533) crystal planes, respectively.[59] To determine the chemical composition and oxidation states of $NiFe_2O_4$, the X-ray photoelectron spectroscopy (XPS) measurements have been performed. In Fig. S4,† the peaks in the full spectrum appear at 712.08, 855.08, and 530.08 electron volts (eV), corresponding to Fe 2p, Ni 2p, and O 1s, respectively, confirming the presence of Fe, Ni, and O elements, consistent with the Energy Dispersive X-ray Spectroscopy (EDS) results shown in Fig. 1d–f. Fig. 2b displays the Fe 2p peaks, which can be deconvoluted into Fe $2p_{3/2}$ and Fe $2p_{1/2}$, positioned at 725.4 and 711.8 eV, respectively.[59] The Ni 2p peaks shown in Fig. 2c can also be deconvoluted into Ni $2p_{3/2}$ and Ni $2p_{1/2}$, positioned at 855.41 and 873.38 eV, respectively.[60] The two sets of fitting peaks around 530.08 and 531.38 eV are attributed to metal–oxygen species and hydroxyl oxygen defects (Fig. 2d). The successful synthesis of $NiFe_2O_4$ is confirmed through the XRD, EDS, and XPS tests, laying a solid foundation for subsequent electrochemical performance evaluations.

3.2. Performance of the electrocatalysts

The performance testing of the prepared catalysts was conducted in an H-type electrochemical cell under ambient conditions. In Fig. 3a, the linear sweep voltammetry (LSV) curves depict the electrochemical performance of Fe MOFs, Fe–Ni LDH, and $NiFe_2O_4$ in a 0.1 mol L^{-1} NaOH solution, with and without the addition of 0.1 mol L^{-1} KNO_3. Notably, all catalysts demonstrate increased current densities upon the introduction of NO_3^-, indicating their efficacy in promoting NO_3^- reduction for NH_3 synthesis. This graph reveals a common trend of all catalysts, showing an increase in current density upon the introduction of NO_3^-. This indicates that NH_3 synthesis through NO_3^- reduction can occur on these catalysts. Simultaneously, the current density of $NiFe_2O_4$ in the figure is significantly higher than those of Fe MOFs and Fe–Ni LDH. This outcome indicates that, for NO_3^-RR, $NiFe_2O_4$ is more active and exhibits superior performance. Fig. 3d and g display the LSV curves of $NiFe_2O_4$ with various nickel source ratios and calcination temperatures in a 0.1 mol L^{-1} NaOH solution, both with and without the addition of 0.1 mol L^{-1} KNO_3. The results indicate that the addition of double amount nickel source and the $NiFe_2O_4$ calcined at 350 °C exhibit higher current density and superior performance. To further investigate the electrocatalytic performance of the catalyst, chronoamperometry measurements (it) were conducted at various potentials in

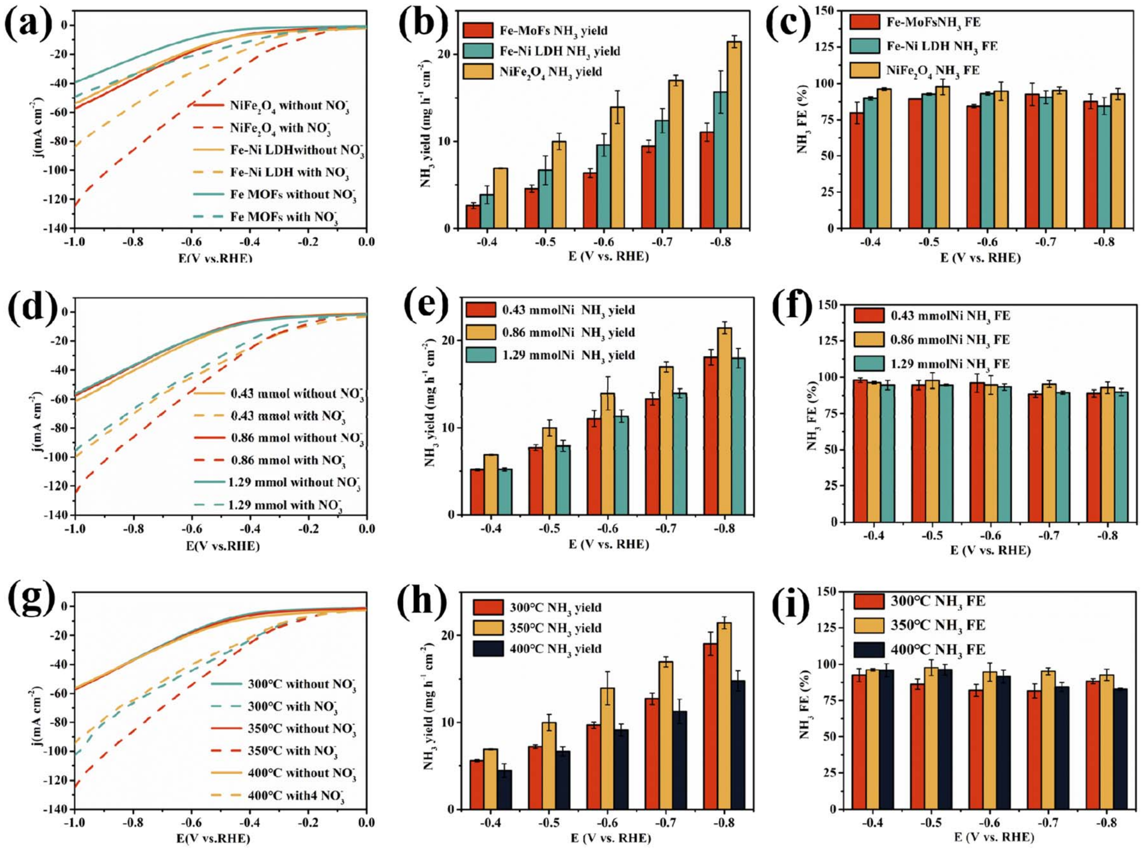

Fig. 3 (a) LSV of the Fe MOFs, Fe–Ni LDH, and $NiFe_2O_4$ in a 0.1 M NaOH solution, with and without the addition of 0.1 M KNO_3. (b and c) NH_3 yield rate and NH_3 FE of the $NiFe_2O_4$ in a 0.1 M NaOH and KNO_3 solution, respectively. (d) LSV of the 0.43 mmol, 0.86 mmol and 1.29 mmol Ni in a 0.1 M NaOH solution, with and without the addition of 0.1 M KNO_3. (e and f) NH_3 yield rate and NH_3 FE of the 0.43 mmol, 0.86 mmol and 1.29 mmol Ni in a 0.1 M NaOH and KNO_3 solution, respectively. (g) LSV of the 300 °C, 350 °C and 400 °C $NiFe_2O_4$ in a 0.1 M NaOH solution, with and without the addition of 0.1 M KNO_3. (h and i) NH_3 yield rate and NH_3 FE of the 300 °C, 350 °C and 400 °C $NiFe_2O_4$ in a 0.1 M NaOH and KNO_3 solution, respectively.

a 30 mL solution containing a mixture of 0.1 mol L^{-1} NaOH and KNO_3. Each measurement was performed for 1 hour at different potentials. When the measurements were completed, the concentration of NH_3 in the catholyte was calculated using the ultraviolet-visible (UV-vis) absorption spectra (Fig. S5a†) and the calibration curve (Fig. S5b†). Fig. 3b and c illustrate the NH_3 yield and FE of three different catalysts: pure MOFs, Fe–Ni LDH, and $NiFe_2O_4$. The NH_3 yield of all three catalysts increase as the potential becomes more negative. When the potential is shifted to −0.8 V (*vs.* RHE), the NH_3 yield for pure MOFs, Fe–Ni LDH, and $NiFe_2O_4$ are 11.05, 15.67, and 21.45 mg h^{-1} cm^{-2}, respectively. The maximum FE for pure MOFs, Fe–Ni LDH, and $NiFe_2O_4$ is 92.54%, 93.00%, and 97.65%, respectively, while the minimum values is 79.71%, 84.62%, and 92.74%. These results indicate that among these three catalysts, $NiFe_2O_4$ demonstrates superior electrocatalytic performance for the NO_3^-RR. To further explore the impact of nickel doping ratio and calcination temperature on the performance of $NiFe_2O_4$, impedance measurements are also conducted on the catalyst at different potentials. As shown in Fig. 3e and f, at a calcination temperature of 350 °C with the amount of nickel at 0.86 mmol (double the amount of nickel), the catalyst exhibits the highest NH_3 yield and FE, reaching maximum values of 21.45 mg h^{-1} cm^{-2} and 97.65%, respectively. This is significantly higher than the case with a single nickel addition (yield: 18.07 mg h^{-1} cm^{-2}, FE: 96.35%) and triple nickel addition (yield: 17.96 mg h^{-1} cm^{-2}, FE: 94.54%). These results indicate that a double amount of nickel represents the optimal ratio. In Fig. 3h and i, under the condition of adding double amount of nickel, the catalyst exhibits the best performance at a calcination temperature of 350 °C (yield: 21.45 mg h^{-1} cm^{-2}, FE: 97.65%). This is significantly superior to the performance at 300 °C (yield: 19.06 mg h^{-1} cm^{-2}, FE: 88.05%) and 400 °C (yield: 14.78 mg h^{-1} cm^{-2}, FE: 92.56%). Through exploration, it is determined that the $NiFe_2O_4$ exhibits the best NO_3^-RR performance when double amount of nickel is added and the calcination temperature is set at 350 °C.

To investigate the selectivity of $NiFe_2O_4$, the concentrations of the main byproducts, NO_2^- and N_2H_4, were detected and calculated by UV-vis (see Fig. S5†). As shown in Fig. 4a, the FE of NO_2^- decreases from 4.5% to 2.3% with the increasing voltage, and the production rate of NO_2^- increases from 0.24 mg h^{-1} cm^{-2} to 0.49 mg h^{-1} cm^{-2}, indicating that the synthesis of NH_3 is accompanied by the generation of trace amounts of NO_2^- at each applied potential. Additionally, the presence of N_2H_4 in the electrolyte was hardly observed (Fig. 4a). Overall, the production of byproducts is negligible compared to the yield and FE of NH_3, indicating that $NiFe_2O_4$ exhibits good selectivity for NO_3^-RR.

Additionally, to demonstrate the source of NH_3, we conducted ^{15}N isotope labeling experiments and cyclic chronoamperometry measurements for seven cycles. As shown in Fig. 4b, in the ^1H nuclear magnetic resonance (NMR) spectra of the electrolyte, after the reaction in the $^{15}NO_3^-$ solution, two peaks corresponding to $^{15}NH_4^+$ are clearly observed. In contrast,

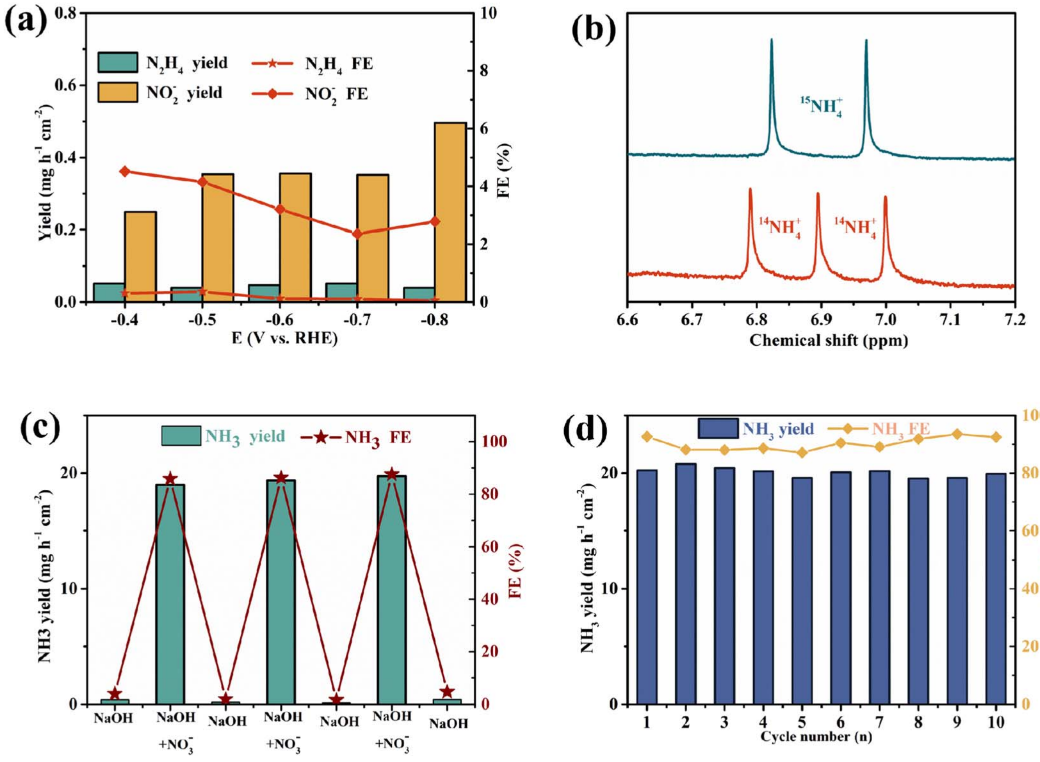

Fig. 4 (a) The yield rate and FE of byproducts NO_2^- and N_2H_4 between −0.4 and −0.8 V for $NiFe_2O_4$. (b) ^1H nuclear magnetic resonance spectrum of the electrolyte after eNO_3^-RR on $NiFe_2O_4$ at −0.8 V with $^{15}NO_3^-$ and $^{14}NO_3^-$ as nitrogen sources. (c) The NH_3 yield rate and FE in alternating cycles between with and without NO_3^- electrolyte of $NiFe_2O_4$ at −0.8 V. (d) 10-Cycle test of $NiFe_2O_4$ at −0.8 V.

when reacting in the $^{14}NO_3^-$ solution, a triplet coupling peak attributed to $^{14}NH_4^+$ is detected. This indicates that the produced NH_3 originates entirely from NO_3^-. As depicted in Fig. 4c, electrolysis experiments are carried out for a total of 7 cycles at −0.8 V *vs.* RHE in 0.1 M NaOH (with and without NO_3^-). The results reveal that NH_3 is solely obtained in the electrolyte containing NO_3^-, providing additional confirmation that the origin of NH_3 is exclusively from NO_3^-.

Stability is a crucial metric for evaluating catalyst performance. We evaluated the stability through a ten-cycle stability test by electrolysis at −0.8 V *vs.* RHE and post-reaction XRD analysis of the catalyst. As shown in Fig. 4d, slight fluctuations can be observed in both NH_3 yield and faradaic efficiency (FE), but they remain around 20 mg h^{-1} cm^{-2} and 90%, respectively. As shown in Fig. S6,† the catalyst material retained its original crystal planes after the reaction, indicating that the catalyst exhibits excellent stability.

3.3. Mechanisms study for NO_3^-RR

To elucidate the excellent performance of $NiFe_2O_4$ in NO_3^-RR and the role of Fe and Ni elements in the reaction, we constructed $NiFe_2O_4$, $Ni_{0.75}Fe_{2.25}O_4$ and $Ni_{1.5}Fe_{1.5}O_4$ molecular models (Fig. S7†) with varying Fe and Ni ratios based on structural characterization results, and performed density functional theory (DFT) calculations along the reaction pathway ($*NO_3 \rightarrow *NO_2 \rightarrow *NO \rightarrow *N \rightarrow *NH \rightarrow *NH_2 \rightarrow *NH_3$). Fig. 5a illustrates the adsorption configurations of the reaction intermediates on $NiFe_2O_4$ during the electrocatalytic process. Furthermore, depicted in Fig. 5b–d, the band gaps for $Ni_{1.5}Fe_{1.5}O_4$, $NiFe_2O_4$, and $Ni_{0.75}Fe_{2.25}O_4$ are 0.29, 0.21, and 0.58 eV, respectively. Notably, $NiFe_2O_4$ displays the narrowest band gap of 0.21 eV, suggesting enhanced conductivity and swifter charge transfer rates in comparison to the other two compositions. The charge density differences shown in Fig. 6a illustrate the electron redistribution at the $NiFe_2O_4$ interface, where Fe and Ni atoms lose electrons (yellow regions), with abundant electron accumulation on NO_3 surface (blue regions), promoting the NO_3^-RR. Substantial electron accumulation on O3 is conducive to the initial hydrogenation–deoxygenation step.

Meanwhile, in this step, as illustrated in Fig. 6b and c, the Fe–O8 bond near the Fe active site remains unchanged, while the Fe–O6 and Fe–O7 bonds elongates slightly from 1.84 to 1.85 Å and 1.85 to 1.86 Å, respectively. In contrast, the length variations of the Ni–O bonds near the Ni active site are more pronounced, with the Ni–O6, Ni–O4, and Ni–O5 bonds elongating from 1.84 to 1.94 Å, 1.84 to 1.91 Å, and 1.85 to 1.95 Å, respectively. For the *NO → *N deoxygenation step, as depicted in Fig. 6f, both Fe and Ni transfer charges to O, leading to distinct charge depletion regions. Also, in this step, as shown in Fig. 6d and e, the Fe–O6 bond elongates from 1.85 to 1.86 Å, while both the Fe–O8 and Fe–O7 bonds shorten from 1.89 to 1.87 Å, and the Fe–N bond shortens from 1.85 to 1.82 Å. The formation of the Ni–N bond is accompanied by the elongation of Ni–O6, Ni–O4, and Ni–O5 bonds from 1.92 to 1.95 Å, 1.88 to 1.96 Å, and 1.89 to 1.96 Å, respectively. Thus, in the bimetallic active site, Fe primarily facilitates charge transfer while Ni contributes predominantly to structural adjustment.

Fig. 6a shows the Gibbs free energy (Δ*G*) diagrams during the NO_3^-RR process on the surface of $NiFe_2O_4$. The first step corresponds to the $*NO_3^-$ adsorption, the Gibbs free energy decreases distinctly for these three catalysts. Especially, it is steeper for the surface with $NiFe_2O_4$, and the free energy of $NiFe_2O_4$ (−2.57 eV) is more favorable for $*NO_3$ adsorption as compared to those of $Ni_{0.75}Fe_{2.25}O_4$ (−1.328 eV) and $Ni_{1.5}Fe_{1.5}O_4$

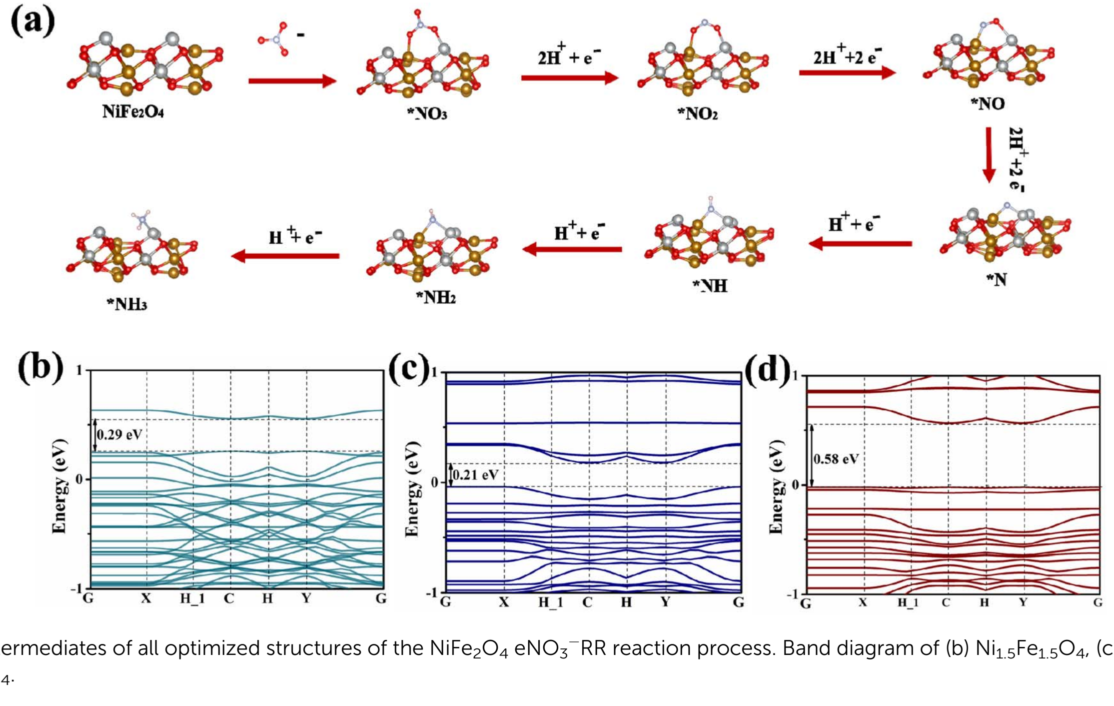

Fig. 5 (a) Intermediates of all optimized structures of the $NiFe_2O_4$ eNO_3^-RR reaction process. Band diagram of (b) $Ni_{1.5}Fe_{1.5}O_4$, (c) $NiFe_2O_4$, (d) $Ni_{0.75}Fe_{2.25}O_4$.

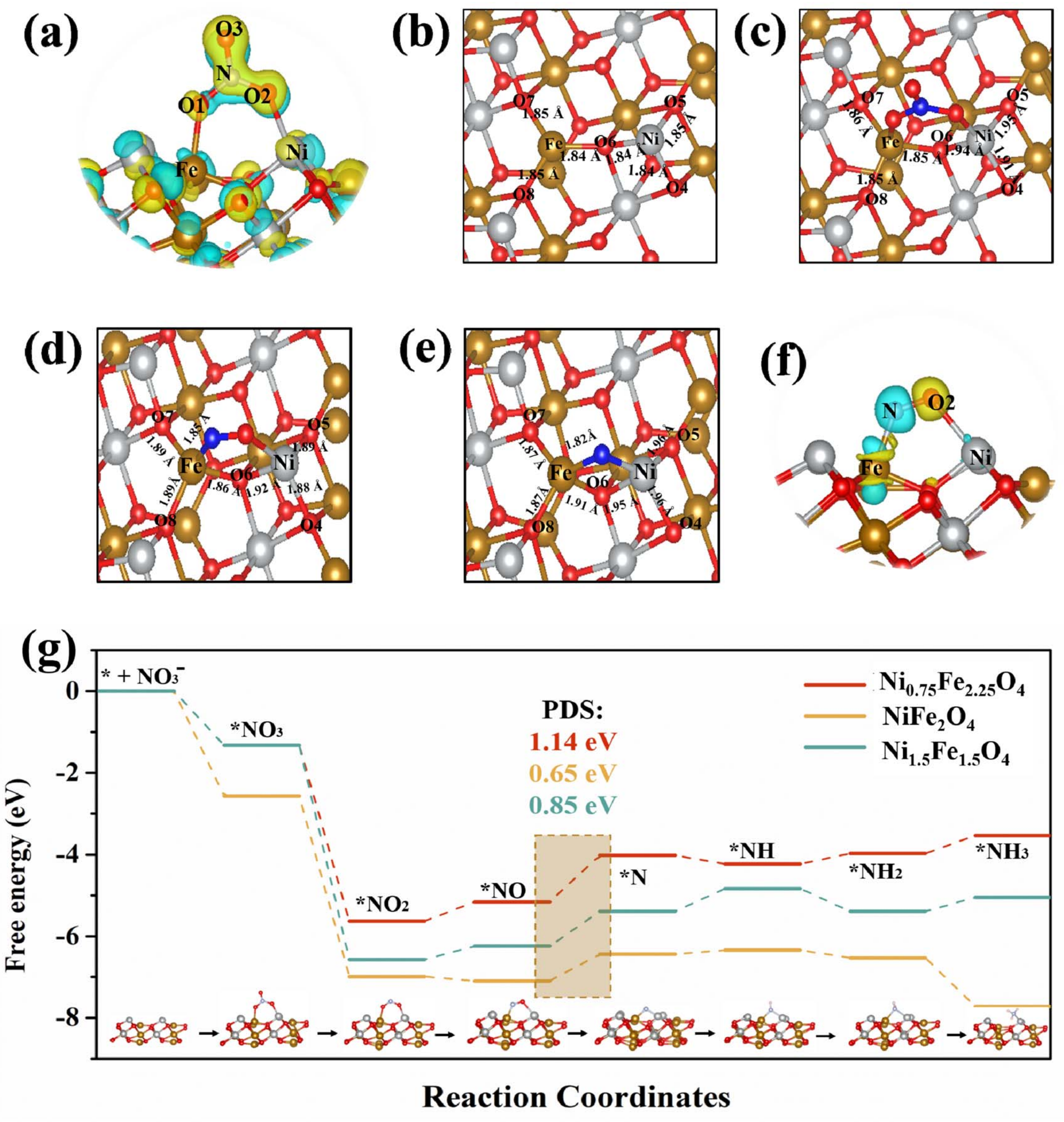

Fig. 6 The charge density differences of (a) $^*NO_3$ and (f) *NO (yellow regions: electrons consumption, blue regions: electrons accumulation). The structural model of (b) $NiFe_2O_4$, (c) $^*NO_3$ with $NiFe_2O_4$, (d) *NO with $NiFe_2O_4$ and (e) *N with $NiFe_2O_4$ (atomic colors represent: golden, Fe; gray, Ni; purple, N; red, O). (g) Free energy changes in each step of the reaction processes on $Ni_{0.75}Fe_{2.25}O_4$, $NiFe_2O_4$, and $Ni_{1.5}Fe_{1.5}O_4$.

(−1.328 eV). A higher energy barrier is observed during the step from *NO to *N, which was identified as the rate-determining step (RDS). The energy barriers for $Ni_{0.75}Fe_{2.25}O_4$, $NiFe_2O_4$, and $Ni_{1.5}Fe_{1.5}O_4$ are −1.14 eV, −0.65 eV, and −0.85 eV, respectively. Therefore, $NiFe_2O_4$ exhibits higher NO_3^-RR activity as compared to $Ni_{1.5}Fe_{1.5}O_4$ and $Ni_{0.75}Fe_{2.25}O_4$.

4. Conclusion

In summary, we successfully synthesized a catalyst ($NiFe_2O_4$) derived from MOFs and investigated their electrocatalytic performance in NO_3^- reduction for NH_3 synthesis. The $NiFe_2O_4$ catalyst prepared with double amount of Ni precursor and subjected to calcination at 350 °C exhibited remarkably high NH_3 production rates and FE in 0.1 M NaOH with 0.1 M NO_3^- solution, reaching maximum values of 21.45 mg h^{-1} cm^{-2} and 97.65%, respectively, at −0.8 V *vs.* RHE. These performance levels significantly surpassed those reported for most catalysts operating under similar conditions. DFT calculations revealed that the $NiFe_2O_4$ catalyst with double amount of Ni precursor is more conducive to reducing the RDS free energy of NO_3^- to NH_3 compared to catalysts with a single or triple amount of Ni precursor, thereby enhancing the performance of NO_3^-RR. Our research provides an attractive approach to addressing wastewater treatment and designing efficient electrochemical NH_3 synthesis catalysts.

Data availability

All relevant data are within the manuscript and its additional files.

Author contributions

J. X., B. L., and S. Y. conceived and designed the project and characterized the catalyst. Y. Z. performed the electrochemical tests and analyzed the data. J. X. performed the DFT calculations and analyzed the corresponding data. J. X., B. L., and S. Y. wrote the first draft. All authors discussed the results, revised the manuscript, and decided on the final version.

Conflicts of interest

There are no conflicts of interest to declare.

Acknowledgements

This work was supported by the Research Foundation for Talented Scholars of Qingdao Agricultural University (No. 6631120039) and National College Student Innovation and Entrepreneurship Training Program (S202010435041). The numerical calculations in this paper were performed on the supercomputing system in the Supercomputing Center of the University of Science and Technology of China. The authors would like to thank Zhao Baobao from Shiyanjia Lab (**https://www.shiyanjia.com**) for the XPS analysis.

References

1 X. Zhong, X. Wu, Y. Liu, S. Yang, H. Li, Q. Wang, D. Shang, F. Du, A. Yuan and F. Yang, *J. Environ. Chem. Eng.*, 2024, **12**, 111871.
2 X. Zhao, Y. Jiang, M. Wang, Y. Huan, Q. Cheng, Y. He, T. Qian and C. Yan, *J. Energy Chem.*, 2024, **92**, 459–483.
3 M. Ye, X. Jiang, Y. Zhang, Y. Liu, Y. Liu and L. Zhao, *Nanomaterials*, 2024, **14**, 102.
4 Y. Chen, C. Yang, H. Li, Z. Ma, D. Wu, Y. Yao, X. Shen and D. Ma, *Chem. Eng. J.*, 2024, **481**, 148857.
5 A. Ma, X. Wu, X. Li, Y. Dewi Susanti, D. Liu, H. Li, A. T. Kuvarega, B. B. Mamba and J. Gui, *Appl. Surf. Sci.*, 2024, **653**, 159397.
6 A. Iqbal, E. Skúlason and Y. Abghoui, *Int. J. Hydrogen Energy*, 2024, **64**, 744–753.
7 S. Zhang, J. Wu, M. Zheng, X. Jin, Z. Shen, Z. Li, Y. Wang, Q. Wang, X. Wang, H. Wei, J. Zhang, P. Wang, S. Zhang, L. Yu, L. Dong, Q. Zhu, H. Zhang and J. Lu, *Nat. Commun.*, 2023, **14**, 3634.
8 B. Xu, D. Li, Q. Zhao, S. Feng, X. Peng and P. K. Chu, *Coord. Chem. Rev.*, 2024, **502**, 215609.
9 H. Liu, J. Timoshenko, L. Bai, Q. Li, M. Rüscher, C. Sun, B. Roldan Cuenya and J. Luo, *ACS Catal.*, 2023, **13**, 1513–1521.
10 X. Fu, *Chin. J. Catal.*, 2023, **53**, 8–12.
11 H. Chen, Z. Zhang, Y. Li, L. Yu, F. Chen and L. Li, *Chem. Eng. J.*, 2024, **481**, 148596.
12 A. Iqbal, E. Skúlason and Y. Abghoui, *J. Phys. Chem. C*, 2024, **128**, 10300–10307.
13 A. Iqbal, E. Skulason and Y. Abghoui, *ChemPhysChem*, 2024, **25**, e202300991.
14 F. Zhao, G. Hai, X. Li, Z. Jiang and H. Wang, *Chem. Eng. J.*, 2023, **461**, 141960.
15 S. Zhang, Y. Zha, Y. Ye, K. Li, Y. Lin, L. Zheng, G. Wang, Y. Zhang, H. Yin, T. Shi and H. Zhang, *Nano-Micro Lett.*, 2024, **16**, 9.
16 Y. Liu, X. Yao, X. Liu, Z. Liu and Y. Wang, *Inorg. Chem.*, 2023, **62**, 7525–7532.
17 A. Iqbal, E. Skúlason and Y. Abghoui, *Crystals*, 2024, **14**, 770.
18 Q. Yao, J. Chen, S. Xiao, Y. Zhang and X. Zhou, *ACS Appl. Mater. Interfaces*, 2021, **13**, 30458–30467.
19 J. Wang, Y. Wang, C. Cai, Y. Liu, D. Wu, M. Wang, M. Li, X. Wei, M. Shao and M. Gu, *Nano Lett.*, 2023, **23**, 1897–1903.
20 Y. Shi, S. Xu and F. Li, *Chem. Commun.*, 2022, **58**, 8714–8717.
21 Y. Luo, K. Chen, G. Wang, G. Zhang, N. Zhang and K. Chu, *Inorg. Chem. Front.*, 2023, **10**, 1543–1551.
22 D. Liu, L. Qiao, Y. Chen, P. Zhou, J. Feng, C. C. Leong, K. W. Ng, S. Peng, S. Wang, W. F. Ip and H. Pan, *Appl. Catal., B*, 2023, **324**, 122293.
23 Y. Zhang, J. Xiong, S. Yan and B. Liu, *J. Electroanal. Chem.*, 2023, **946**, 117702.
24 J. Zhao, L. Liu, Y. Yang, D. Liu, X. Peng, S. Liang and L. Jiang, *ACS Sustainable Chem. Eng.*, 2023, **11**, 2468–2475.
25 S. Meng, Y. Ling, M. Yang, X. Zhao, A. I. Osman, A. A. H. Al-Muhtaseb, D. W. Rooney and P. Yap, *J. Environ. Chem. Eng.*, 2023, **11**, 109418.
26 H. Wang, D. Zhao, C. Liu, X. Fan, Z. Li, Y. Luo, D. Zheng, S. Sun, J. Chen, J. Zhang, Y. Liu, S. Gao, F. Gong and X. Sun, *J. Mater. Chem. A*, 2022, **10**, 24462–24467.
27 Y. Cao, S. Yuan, L. Meng, Y. Wang, Y. Hai, S. Su, W. Ding, Z. Liu, X. Li and M. Luo, *ACS Sustainable Chem. Eng.*, 2023, **11**, 7965–7985.
28 C. Ma, H. Zhang, J. Xia, X. Zhu, K. Qu, F. Feng, S. Han, C. He, X. Ma, G. Lin, W. Cao, X. Meng, L. Zhu, Y. Yu, A. Wang and Q. Lu, *J. Am. Chem. Soc.*, 2024, **146**, 20069–20079.
29 Y. Kim, J. Ko, M. Shim, J. Park, H. Shin, Z. H. Kim, Y. Jung and H. R. Byon, *Chem. Sci.*, 2024, **15**, 2578–2585.
30 J. Cheng, G. Dai, W. Sun, X. Yang, R. Xia, Y. Xu and Y. Mao, *Energy Fuels*, 2024, **38**, 2501–2510.
31 Y. Wang, S. Wang, Y. Fu, J. Sang, Y. Zang, P. Wei, H. Li, G. Wang and X. Bao, *Chin. J. Catal.*, 2024, **56**, 104–113.
32 K. Huang, K. Tang, M. Wang, Y. Wang, T. Jiang and M. Wu, *Adv. Funct. Mater.*, 2024, **24**, 2315324.
33 C. Wang, Y. Zhang, H. Luo, H. Zhang, W. Li, W. X. Zhang and J. Yang, *Small Methods*, 2022, **6**, 2200790.
34 S. Yuan, Y. Xue, R. Ma, Q. Ma, Y. Chen and J. Fan, *Sci. Total Environ.*, 2023, **866**, 161444.
35 Q. Song, M. Li, X. Hou, J. Li, Z. Dong, S. Zhang, L. Yang and X. Liu, *Appl. Catal., B*, 2022, **317**, 121721.
36 Y. Li, X. Tan, R. K. Hocking, X. Bo, H. Ren, B. Johannessen, S. C. Smith and C. Zhao, *Nat. Commun.*, 2020, **11**, 2720.
37 M. Fu, Q. Gou, Z. Ma, Y. Jiang, W. Shen, M. Li and R. He, *Appl. Surf. Sci.*, 2024, **643**, 158664.
38 W. Yu, J. Yu, M. Huang, Y. Wang, Y. Wang, J. Li, H. Liu and W. Zhou, *Energy Environ. Sci.*, 2023, **16**, 2991–3001.
39 R. Zhao, Y. Wang, G. Ji, J. Zhong, F. Zhang, M. Chen, S. Tong, P. Wang, Z. Wu, B. Han and Z. Liu, *Adv. Mater.*, 2023, **35**, 2205262.

40 P. Liu, J. Yan, H. Huang and W. Song, *Chem. Eng. J.*, 2023, **466**, 143134.

41 J. Sun, W. Gao, H. Fei and G. Zhao, *Appl. Catal., B*, 2022, **301**, 120829.

42 F. Wang, Z. Zhang, C. Wang, X. Yi and S. Yi, *Sep. Purif. Technol.*, 2024, **337**, 126409.

43 S. Zhang, M. Li, J. Li, Q. Song and X. Liu, *Proc. Natl. Acad. Sci. U. S. A.*, 2022, **119**, e2115504119.

44 X. Wang, L. Chai, J. Ding, L. Zhong, Y. Du, T. Li, Y. Hu, J. Qian and S. Huang, *Nano Energy*, 2019, **62**, 745–753.

45 R. Lin, L. Mao, Y. Ding and J. Qian, *Chem. Commun.*, 2023, **59**, 12875–12878.

46 A. Ashoori, A. Noori, M. S. Rahmanifar, A. Morsali, N. Hassani, M. Neek-Amal, H. Ghasempour, X. Xia, Y. Zhang, M. F. El-Kady, R. B. Kaner and M. F. Mousavi, *ACS Appl. Mater. Interfaces*, 2023, **15**, 30220–30239.

47 T. Lan, H. Du, Y. Li, K. Qu, J. Zhao, X. Zhang, Y. Dong, Y. Zhang, X. Zhang and D. Zhang, *J. Alloys Compd.*, 2023, **943**, 169144.

48 Q. Shao, J. Yang and X. Huang, *Chem.–Eur. J.*, 2018, **24**, 15143–15155.

49 B. Y. Guan, L. Yu and X. W. D. Lou, *Angew. Chem., Int. Ed.*, 2017, **56**, 2386–2389.

50 L. Zhang, H. B. Wu and X. W. D. Lou, *J. Am. Chem. Soc.*, 2013, **135**, 10664–10672.

51 D. Chen, Q. Sun, C. Han, Y. Guo, Q. Huang, W. A. Goddard and J. Qian, *J. Mater. Chem. A*, 2022, **10**, 16007–16015.

52 D. Kong, Y. Wang, S. Huang, J. Hu, Y. V. Lim, B. Liu, S. Fan, Y. Shi and H. Y. Yang, *Energy Storage Mater.*, 2019, **23**, 653–663.

53 X. Liu, X. Cui, K. Dastafkan, H. Wang, C. Tang, C. Zhao, A. Chen, C. He, M. Han and Q. Zhang, *J. Energy Chem.*, 2021, **53**, 290–302.

54 J. Li, D. Zhao, L. Zhang, Y. Ren, L. Yue, Z. Li, S. Sun, Y. Luo, Q. Chen, T. Li, K. Dong, Q. Liu, Q. Kong and X. Sun, *J. Colloid Interface Sci.*, 2023, **629**, 805–812.

55 L. Xie, L. Hu, Q. Liu, S. Sun, L. Zhang, D. Zhao, Q. Liu, J. Chen, J. Li, L. Ouyang, A. A. Alshehri, Q. Kong and X. Sun, *Inorg. Chem. Front.*, 2022, **9**, 3392–3397.

56 Y. Zhang, J. Xiong, B. Liu and S. Yan, *J. Colloid Interface Sci.*, 2024, **662**, 39–47.

57 G. Kresse and J. Furthmüller, *Comput. Mater. Sci.*, 1996, **6**, 15–50.

58 C. Ma, D. Liu, Y. Zhang, J. Yong Lee, J. Tian, B. Liu and S. Yan, *Chem. Eng. J.*, 2022, **430**, 132694.

59 S. Shaheen, S. Xu, J. Bian, A. Zada, Z. Zhang, Y. Qu and L. Jing, *Rare Met.*, 2024, **43**, 1580–1588.

60 Q. Yao, J. Chen, S. Xiao, Y. Zhang and X. Zhou, *ACS Appl. Mater. Interfaces*, 2021, **13**, 30458–30467.